Nonresonant inelastic x-ray scattering from actinides and rare earths

G. van der Laan
Diamond Light Source, Chilton, Didcot, Oxfordshire OX11 0DE, United Kingdom
(Received 14 May 2012; published 23 July 2012)

Calculated multiplet spectra are presented for the electric-multipole transitions in nonresonant inelastic x-ray scattering (NIXS) at the $O_{4,5}$ edges of actinides and the $N_{4,5}$ edges of rare earths. The multiplet structure is characteristic for the f count as well as for the angular momentum coupling. As a remarkable peculiarity, the calculations for the actinide $O_{4,5}$ edge show that the higher multipole spectra resemble jj coupling, whereas the dipole spectrum is close to LS coupling. The exchange integral $G^1(5d,5f)$ is responsible for a shift of ~15 eV of the dipole spectrum to higher energy. This high energy is conserved by a sum rule for the average energy of the accessible final states. In the higher multipole spectra, where the allowed final states are different, the splitting by the $5d$ spin-orbit interaction exceeds that of the electrostatic interaction. This leads to a distinct spin-orbit-split doublet structure, with a broad first peak and a narrower second peak. According to the spin-orbit sum rule, the $5f$ spin-orbit interaction per hole is linearly related to the core-level branching ratio, where the proportionality factor is opposite in sign for the $k = 3$ and 5 spectra. Compared to the $k = 3$ spectrum, the $k = 5$ spectrum has overall a lower intensity in the low-energy region but a higher intensity in the high-energy region, especially for the heavier elements in the series. The NIXS at the rare-earth $N_{4,5}$ edge is quite different since the electrostatic and core spin-orbit splitting in the $k = 3$ and 5 spectra are of similar size. The pre-edge region of the rare-earth spectra, where the linewidth is narrow, shows a rich multiplet structure that depends strongly on the initial-state J value.

DOI: 10.1103/PhysRevB.86.035138 PACS number(s): 78.70.Ck, 71.70.Ej, 71.10.−w, 31.15.am

I. INTRODUCTION

Nonresonant inelastic x-ray scattering (NIXS) is emerging as a useful bulk-sensitive probe to study the electronic structure in strongly correlated materials.[1] NIXS is a photon-in–photon-out technique, which has clear advantages over measurements using electron detection. While the low-energy loss spectrum shows collective excitations, such as plasmons and phonons, the high-energy loss spectrum displays core excitations and Compton scattering. Here, we will discuss uniquely the shallow core excitations observed in hard x-ray scattering from actinides and rare earths, which have relatively high cross sections. Among the advantages of using hard x rays instead of soft x rays are access to extreme conditions, bulk sensitivity, and an almost unlimited momentum transfer. Whereas electric-dipole transitions prevail at low photon energies, the availability of high-energy synchrotron radiation has enabled the exploration of the higher multipole transitions. These transitions prevail at high momentum transfer and give complementary information compared to the electric-dipole transitions measured by x-ray absorption spectroscopy (XAS) or electron energy loss spectroscopy (EELS), hence provide information on the electronic configuration and local environment, such as valence state, site symmetry, and hybridization.[1–6] Compared to resonant inelastic x-ray scattering, NIXS loses out on count rate, however, this is often largely compensated by an unambiguous interpretation in terms of a first-order process instead of more complicated coherent second-order processes.

Very recently, a spin-orbit sum rule for the electric-multipole transitions in NIXS was derived, which gives a linear relation between the spin-orbit-split branching ratio of the core-level spectrum and the angular part of the initial-state spin-orbit interaction per hole.[7]

Actinide elements and their compounds are only modestly understood, and questions remain concerning the number of $5f$ electrons, valence state, and angular momentum coupling, which all play a major role in the magnetic and electronic properties of these materials.[8,9] Recent studies of the actinide chemical bonding are leading a revision of previous notions of valence state and electronic orbital mixing, thus putting a premium on experimental methods sensitive to the valence electronic structure and low-energy electronic excited states.[10–13] Rare-earth materials form an integral component in a wide range of modern technologies, such as wind turbines, hybrid-car engines, visual displays, and lasers.

Recently, Caciuffo *et al.*[5] reported a strong NIXS at the $O_{4,5}$ in uranium compounds, associated with the electronic transition $5f^n + \hbar\omega_i \rightarrow 5d^9 5f^{n+1} + \hbar\omega_f$. For small values of the scattering vector q, the spectrum is dominated by dipole-allowed transitions encapsulated within the ill-defined giant resonance, which shows good agreement with XAS and EELS measurements.[8,14,15] At higher q values, the higher multipole transitions give strong and well-defined multiplet peaks in the pre-edge region. A similar behavior is found for NIXS at the $N_{4,5}$ edges of rare earths.[6]

The inelastic scattering cross section is large between shells of the same principal quantum number, i.e., for the $nd \rightarrow nf$ transitions, such as the rare-earth $N_{4,5}$ ($4d \rightarrow 4f$) and actinide $O_{4,5}$ ($5d \rightarrow 5f$) edges, especially when the nf electrons are localized. In contrast, the $(n-1)d \rightarrow nf$ transitions are much weaker because of the reduced radial overlap of initial- and final-state wave functions, and also they require a higher momentum transfer q. So far, NIXS experiments did not reveal the actinide $N_{4,5}$ ($4d \rightarrow 5f$) edges[5] and for the rare-earth $M_{4,5}$ ($3d \rightarrow 4f$) edges only the $k = 1$ spectra could be observed.[6] Comparison of the experimental NIXS with calculated spectra have shown no evidence that the rare-earth $M_{4,5}$ spectra contain significant amounts of higher multipole contributions at the measured q range from 2.2–5.8 a.u. The absence of these

higher multipole contributions can be ascribed to the smaller radius of the $3d$ core orbitals, compared to the $4d$, which shifts the maximum intensity of the individual multipole transitions to higher q, so that the region where $k = 3$ and 5 scattering is dominant is also a region of very low NIXS intensity.[6]

In this paper, we use many-electron multiplet theory to calculate the actinide and rare-earth transitions in XAS, EELS, and NIXS. There have been attempts to interpret the actinide $O_{4,5}$ spectra either with spin-orbit interaction[16] or electrostatic interactions,[17] but here we will show that it is essential to take both interactions into account. The multiplet structure is spread over a region of up to 20 eV, which is comparable to the $5d$ spin-orbit splitting (≈8.2 eV). Hence, a model that relies primarily on electrostatic interactions would fail to describe all features. In fact, it turns out to be quite the opposite. We demonstrate that spin-orbit interaction plays a dominant role in the higher multipole spectra.

The outline of this paper is as follows. Section II gives a general theoretical description for the NIXS transitions and makes a comparison with XAS. Section III provides a step-by-step derivation of the allowed transitions and associated intensities in the different multipole spectra for the transition $f^0 \rightarrow d^9 f^1$, in which spin-orbit and electrostatic interactions are taken on equal footing. This rather straightforward calculation provides deeper insight into the origin of the various spectral features. Section IV presents many-electron calculations for the actinide $O_{4,5}$ spectra. It compares the results in intermediate coupling with those in the LS- and jj-coupling limits, which facilitates the analysis of the spectral structure. Section V makes a comparison with the rare-earth $N_{4,5}$ multipole spectra. Section VI gives the summary and conclusions.

II. THEORY

A. Multipolar expansion of NIXS

In the relativistic photon-matter interaction Hamiltonian $\mathcal{H}_{\rm int}$, the leading terms containing explicitly the vector potential $\mathbf{A}$ are[1,18]

$$\mathcal{H}_{\rm int} = \sum_{n=1}^{N}\left[\frac{e}{mc}\mathbf{A}(\mathbf{k},\mathbf{r}_n)\cdot\mathbf{p}_n + \frac{e^2}{2mc}\mathbf{A}^2(\mathbf{k},\mathbf{r}_n) + \frac{e\hbar}{2mc}\sigma_n\cdot\nabla\times\mathbf{A}(\mathbf{k},\mathbf{r}_n) + \ldots\right], \quad (1)$$

where $\mathbf{r}_n$ and $\mathbf{p}_n$ are the position vector and momentum operator of the nth electron, respectively, $\mathbf{k}$ is the photon wave vector, e is the elementary charge, m is the electron rest mass, and c is the speed of light. The first two terms arise from the expansion of the kinetic energy operator $\frac{1}{2m}(\mathbf{p} - \frac{e}{c}\mathbf{A})^2$, while the third one comes out of the Dirac equation, where σ_n is the spin vector operator, the components of which are the Pauli matrices. For brevity, we will omit the summation over n in the following.

The $\mathbf{A}\cdot\mathbf{p}$ term in Eq. (1) gives the resonant electric-multipole scattering, including XAS and resonant inelastic scattering (RIXS), the $\mathbf{A}^2$ term gives the nonresonant scattering, and the $\sigma\cdot\nabla\times\mathbf{A} = \sigma\cdot\mathbf{B}$ term gives the magnetic scattering, which is much smaller. At incident photon energies far away from resonant excitation, the double differential cross section (DDCS) for inelastic x-ray scattering is usually derived in the Born approximation.[1,5–7,19] Applying Fermi's golden rule to the $\mathbf{A}^2$ term and writing the vector potential as

$$\mathbf{A}(\mathbf{k},\mathbf{r}) = \hat{\varepsilon}(\mathbf{k})e^{i\mathbf{k}\cdot\mathbf{r}}, \quad (2)$$

where $\hat{\varepsilon}(\mathbf{k})$ is the photon polarization vector, the DDCS is obtained as

$$\frac{d^2\sigma}{d\Omega\, d\omega} = \left(\frac{d\sigma}{d\Omega}\right)_{\rm Th} S(\mathbf{q},\omega), \quad (3)$$

with the dynamical structure factor

$$S(\mathbf{q},\omega) = \sum_f |\langle f|e^{i\mathbf{q}\cdot\mathbf{r}}|i\rangle|^2\delta(E_i - E_f + \hbar\omega), \quad (4)$$

and geometrical factor

$$\left(\frac{d\delta}{d\Omega}\right)_{\rm Th} = r_0^2\,\frac{\omega_f}{\omega_i}|\hat{\varepsilon}_f^*(\mathbf{k}_f)\cdot\hat{\varepsilon}_i(\mathbf{k}_i)|^2, \quad (5)$$

where $\hbar\omega = \hbar\omega_i - \hbar\omega_f$ is the energy transfer, $\mathbf{q} = \mathbf{k}_i - \mathbf{k}_f$ is the momentum transfer in the excitation process, $|i\rangle$ and $\langle f|$ are the initial and final multielectronic states of the target (with associated energies E_i and E_f), and r_0 is the classical electron radius.

In Eq. (3), the Thomson differential scattering cross section $(d\sigma/d\Omega)_{\rm Th}$ is factored out of the DDCS, so that the technique measures a target excitation structure known as the dynamic structure factor $S(\mathbf{q},\omega)$, which is independent of the specific experiment. In the case of EELS, one uses the Rutherford electron scattering cross section

$$\left(\frac{d\delta}{d\Omega}\right)_{\rm Ru} = \frac{4}{q^4}\,\frac{p_f}{p_i}, \quad (6)$$

where p_i (p_f) is the momentum of the incoming (scattered) electron.

The transition operator $e^{i\mathbf{q}\cdot\mathbf{r}}$ in the dynamical structure factor can be expanded in a sum over scalar products of spherical multipole tensors with rank k and components $\kappa = -k,\ldots,k$ as

$$e^{i\mathbf{q}\cdot\mathbf{r}} = \sum_{k,\kappa} i^k(2k+1)j_k(qr)C_\kappa^{(k)*}(\hat{\mathbf{q}})\cdot C_\kappa^{(k)}(\hat{\mathbf{r}}), \quad (7)$$

where $j_k(qr)$ is the kth-order spherical Bessel function and $C_\kappa^{(k)}(\hat{\mathbf{r}}) = \sqrt{4\pi/(2k+1)}\,Y_\kappa^{(k)}(\hat{\mathbf{r}})$ are the renormalized spherical harmonics.

Assuming isotropic sample conditions, interference terms ($k \neq k'$) vanish. With the radial-matrix elements constant over the spectral region of interest, $S(\mathbf{q},\omega)$ can be separated into an angular and a radial part. The angular part of the isotropic 2^k-pole spectrum is

$$I^k(\omega) = \sum_{f,\kappa}|\langle f|C_\kappa^{(k)}(\hat{\mathbf{r}})|i\rangle|^2\delta(E_i - E_f + \hbar\omega). \quad (8)$$

Multipole moments k for the $\ell \rightarrow \ell'$ transition are restricted by the triangle condition $|\ell - \ell'| \leqslant k \leqslant \ell + \ell'$ and parity rule $\ell + \ell' + k =$ even. Thus, for $d \rightarrow f$ transitions, $k =$ 1 (dipole), $k = 3$ (octupole), and $k = 5$ (triakontadipole) transitions are allowed.

B. Comparison with XAS

At low momentum transfer ($q \to 0$), as in the case of soft XAS or EELS, only dipole transitions are important. In the dipole approximation, the XAS spectrum for $f^n + \hbar\omega \to d^9 f^{n+1}$ is the same as the NIXS spectrum for $f^n + \hbar\omega_i \to d^9 f^{n+1} + \hbar\omega_f$.

XAS arises from the $\mathbf{A}\cdot\mathbf{p}$ term in $\mathcal{H}_{\rm int}$. Converting the matrix elements to the length form by using the equation of motion

$$\mathbf{p} \equiv -i\hbar\nabla = \frac{m}{i\hbar}\,[\mathbf{r},\mathcal{H}_0]\,, \tag{9}$$

where $\mathcal{H}_0$ is the ground-state Hamiltonian, and expanding the vector potential [cf. Eq. (2)] gives

$$\langle f|\mathbf{A}\cdot\mathbf{p}|i\rangle = i\,m(E_f - E_i)\langle f|(\hat{\varepsilon}\cdot\mathbf{r})e^{i\mathbf{k}\cdot\mathbf{r}}|i\rangle. \tag{10}$$

For low momentum transfer $(\mathbf{k}\cdot\mathbf{r}) \ll 1$, the exponential in the matrix element can be expanded as

$$e^{i\mathbf{k}\cdot\mathbf{r}} = 1 + i\mathbf{k}\cdot\mathbf{r} - \tfrac{1}{2}(\mathbf{k}\cdot\mathbf{r})^2 + \ldots, \tag{11}$$

and the leading terms in the transition amplitude are

$$-\frac{m}{\hbar}(E_f - E_i)\left[\langle f|\hat{\varepsilon}\cdot\mathbf{r}|i\rangle + \frac{i}{2}\langle f|(\hat{\varepsilon}\cdot\mathbf{r})(\mathbf{k}\cdot\mathbf{r})|i\rangle\right] - \langle f|(\mathbf{k}\times\hat{\varepsilon})(\mathbf{L} + g\mathbf{S})|i\rangle + \ldots, \tag{12}$$

where the first, second, and third terms represent the electric dipole (E1), quadrupole (E2), and magnetic-dipole (M1) transition matrix elements, respectively. The E2 and M1 transition probabilities are $(\alpha Z_{\rm eff})^2$ times smaller than that of E1, where α is the fine-structure constant $e^2/\hbar c \approx 1/137$.

The transition operator $(\hat{\varepsilon}\cdot\mathbf{r})e^{i\mathbf{k}\cdot\mathbf{r}}$ can be recoupled to sum over spherical-tensor products

$$\sum_L \left[[C^{(1)}(\hat{\varepsilon}), C^{(L-1)}(\hat{\mathbf{k}})]^{(L)}_\lambda, C^{(L)}_\lambda(\hat{\mathbf{r}})\right]^{(0)}_0, \tag{13}$$

with the couplings defined by

$$[C^{(L')}, C^{(L'')}]^{(L)}_\lambda \equiv \sum_{\lambda'\lambda''} C^{(L')}_{\lambda'} C^{(L'')}_{\lambda''} C^{L\lambda}_{L'\lambda',L''\lambda''}, \tag{14}$$

where $C^{L\lambda}_{L'\lambda',L''\lambda''}$ is a Clebsch-Gordan coefficient.

The factor $C^{(L)}_\lambda(\hat{\mathbf{r}})$ in Eq. (13), which can be separated from the geometrical part, describes the dynamical part, gives the same isotropic spectra $I^L(\omega)$ as in NIXS [cf. Eq. (8)]. Expressions for the geometric and dynamical part of the electric- and magnetic-multipole transitions of arbitrary rank can be found in Ref. 20.

The reason that XAS and NIXS give the same spectra, despite different transition-matrix elements, is provided by the concept of the fundamental spectra, where the angular part of the transition probability is separated from the radial and geometrical parts.[21,22] A requirement for this is that the radial part remains constant over the spectral range, which is usually fulfilled. This concept is a general principle, and can lead to striking connections, e.g., in core-level photoemission the magnetic linear dichroism in the angular dependence gives the same spectrum as the magnetic circular dichroism.[23]

For the electric dipole ($L = 1$), the $\hat{\mathbf{k}}$ dependence is absent, and the transition operator is

$$\hat{\varepsilon}\cdot\mathbf{r} = \sum_{j=x,y,z} \hat{\varepsilon}_j r_j = r \sum_{\lambda=-1,0,1} C^{(1)*}_\lambda(\hat{\varepsilon})\cdot C^{(1)}_\lambda(\hat{\mathbf{r}}). \tag{15}$$

Thus, in the dipole approximation, $\hat{\varepsilon}$ in XAS plays the same role as $\hat{\mathbf{q}}$ in NIXS. However, it should be noted that $\hat{\varepsilon}$ is an axial vector, allowing anti-Hermitian matrix elements and hence x-ray magnetic circular dichroism (XMCD),[24] whereas $\hat{\mathbf{q}}$ is a polar vector allowing only Hermitian matrix elements. Contrary to XAS, it is easy in NIXS to reach the range $qa \gtrsim 1$, where a is the atomic radius, enabling dipole-forbidden transitions with high probability, by increasing the scattering angle θ and thereby shifting $q = 2(\mathbf{k}_i - \mathbf{k}_f)\sin\theta$.

C. Multiplet calculations

The calculated multipole spectra defined in Eq. (8) will be presented in the following sections. In Sec. III, calculations for transitions from a closed shell to a two-particle final state are performed step by step in order to provide a deeper insight into the origin of the spectral features. Many-electron systems containing more than two particles can be calculated using Racah algebra, including coefficients of fractional parentage and seniority numbers when two or more terms have the same LS value. In Sec. IV, transition probabilities for angle-integrated electric 2^k-pole transitions $f^n \to d^9 f^{n+1}$ are obtained using atomic multiplet calculations in spherical symmetry.[20] The wave functions of the initial- and final-state configurations are calculated in intermediate coupling using Cowan's atomic Hartree-Fock (HF) code with relativistic correction.[25]

The HF values of the Slater parameters are reduced to 70% for actinides and 80% for rare earths to account for configuration interaction and screening effects. Such a reduction was previously found as the optimal value for the rare-earth $M_{4,5}$ XAS.[20,26] The calculated actinide $O_{4,5}$ and rare-earth $N_{4,5}$ spectra were broadened with a Lorentzian of half-width $\Gamma = 0.5$ and 0.1 eV, respectively, to conform to previous experimental work.[5,6,8] The energy resolution of the $k = 3$ and 5 transitions in the experimental rare-earth $N_{4,5}$ spectra is usually limited by the instrumental broadening and not by the intrinsic linewidth, which is expected to be the same as in the pre-edge of the dipole spectrum. A good agreement for the giant-resonance structure in the dipole spectra can be obtained by convolution of the peaks with a Fano line shape of half-width $\Gamma = 4$–6 eV and asymmetry parameter $q = 4$–2.5.[27–29]

III. $f^0 \to d^9 f^1$ TRANSITION

As a case of manageable size, the multipole spectra of the $f^0 \to d^9 f^1$ transition are derived step by step in intermediate coupling, which takes into account both spin-orbit and electrostatic interactions. The results provide useful insight into the origin of the multiplet structure.

TABLE I. Final states of the d^9f^1 configuration. From the initial state $^1S_0$, only the singlet final states can be reached in LS coupling with selection rules $\Delta S = 0$ and $\Delta L = \Delta J = k$. In intermediate coupling, the singlet state mixes with triplet states of the same J value. In jj coupling, the $j_d j_f$ states with $|j_d - j_f| \leqslant J \leqslant j_d + j_f$ can be reached. Each J block has the same number of $j_d j_f$ as LS states.

	Allowed $^{2S+1}L_J$ states		
J	Singlet	Triplet	Allowed jj states
0		$^3P_0$	$d_{5/2}f_{5/2}$
1	$^1P_1$	$^3P_1$, $^3D_1$	$d_{3/2}f_{5/2}$,$d_{5/2}f_{5/2}$,$d_{5/2}f_{7/2}$
2	$^1D_2$	$^3P_2$, $^3D_2$, $^3F_2$	$d_{3/2}f_{5/2}$,$d_{3/2}f_{7/2}$,$d_{5/2}f_{5/2}$,$d_{5/2}f_{7/2}$
3	$^1F_3$	$^3D_3$, $^3F_3$, $^3G_3$	$d_{3/2}f_{5/2}$,$d_{3/2}f_{7/2}$,$d_{5/2}f_{5/2}$,$d_{5/2}f_{7/2}$
4	$^1G_4$	$^3F_4$, $^3G_4$, $^3H_4$	$d_{3/2}f_{5/2}$,$d_{3/2}f_{7/2}$,$d_{5/2}f_{5/2}$,$d_{5/2}f_{7/2}$
5	$^1H_5$	$^3G_5$, $^3H_5$	$d_{3/2}f_{7/2}$,$d_{5/2}f_{5/2}$,$d_{5/2}f_{7/2}$
6		$^3H_6$	$d_{5/2}f_{7/2}$

A. Allowed multipole transitions

The initial state f^0 is $^1S_0$. The final state d^9f^1 configuration has a total number of $LSJM_J$ levels equal to $(4\ell+2)(4\ell'+2) = 140$, where ℓ, L, S, J, and M_J are the azimuthal, orbital, spin, angular momentum, and magnetic quantum numbers, respectively. Accounting for the degeneracy in M_J (where $-J \leqslant M_J \leqslant J$) in the absence of magnetic and crystal fields gives 20 different LSJ states. These are the $^{2S+1}L_J$ states with $|\ell_d - \ell_f| \leqslant L \leqslant \ell_d + \ell_f$, $S = 0,1$, and $|L - S| \leqslant J \leqslant L + S$, listed in Table I, where they are separated in singlet and triplet states. In LS coupling, electric 2^k-pole transitions from $^1S_0$ are allowed to final states with $S = 0$ and $J = L = k$. This limits the number of allowed LS states to one for each k.

In intermediate coupling, only J is a good quantum number, and $J = k$ due to the absence of angular momentum in the initial state. The spin-orbit interaction mixes the singlet $L = k$ state with triplet states that have $k-1 \leqslant L \leqslant k+1$. If all multipole transitions would be allowed, all final states of the d^9f^1 configuration could be reached, however, parity conservation permits only odd k.

In jj coupling, $j_d = \{3/2,5/2\}$ and $j_f = \{5/2,7/2\}$ levels can have J values with $|j_d - j_f| \leqslant J \leqslant j_d + j_f$, which are listed in Table I. Since J is a good quantum number, each J block contains the same number of $j_d j_f$ as LS states. Since $J = k$, each multipole spectrum corresponds to a unique J block.

B. Electrostatic interaction

Having established the allowed final states of each k spectrum in the various coupling schemes, we now turn our attention to the energy positions of these final states, which are split by electrostatic and spin-orbit interaction. The electrostatic interaction for the LS state is given by the two-particle integral

$$\begin{aligned}\langle n\ell,n'\ell';LS|\frac{e^2}{r_{12}}|n\ell,n'\ell';LS\rangle &= E_{\rm av} + \sum_{k>0} f_k(\ell,\ell';L)F^k(n\ell,n'\ell') \\ &+ \sum_k g_k(\ell,\ell';LS)G^k(n\ell,n'\ell'),\end{aligned} \tag{16}$$

TABLE II. Values of the coefficients f_k and g_k for d^9f^1 using Eqs. (17) and (18), with the boldface numbers for singlet states with $L = k$. The last column gives the final-state energies (in eV) using the Slater parameters for U $5d^95f^1$ from Table III scaled to 70% and without spin-orbit interaction.

	f_2	f_4	g_1	g_3	g_5	$E(N_{4,5})$
$^3P_1$	$-8/35$	$-2/21$	$-3/70$	$-2/105$	$-5/231$	-2.979
$^3H_5$	$-2/21$	$-1/231$	$-3/70$	$-2/105$	$-5/231$	-1.418
$^3D_{1,3}$	$-2/35$	$1/7$	$-3/70$	$-2/105$	$-5/231$	-0.332
$^3F_3$	$11/105$	$-2/21$	$-3/70$	$-2/105$	$-5/231$	-0.278
$^1H_5$	$-2/21$	$-1/231$	$-3/70$	$-2/105$	$\mathbf{215/847}$	-0.228
$^3G_{3,5}$	$1/7$	$2/63$	$-3/70$	$-2/105$	$-5/231$	$+0.701$
$^1F_3$	$11/105$	$-2/21$	$-3/70$	$\mathbf{38/105}$	$-5/231$	$+2.021$
$^1P_1$	$-8/35$	$-2/21$	$\mathbf{137/70}$	$-2/105$	$-5/231$	$+16.404$

where f_k and g_k are the angular coefficients, and F^k and G^k the radial integrals of the Coulomb and exchange integrals, respectively, where k refers here to the multipole rank of the electrostatic interaction (and not the rank of the transition operator). $E_{\rm av}$ is the spherically averaged electrostatic energy.

For $\underline{\ell}\ell'$ ($=\ell^{4\ell+1}\ell'$), i.e., one hole, denoted by an underscore, in the ℓ shell and one electron in the ℓ' shell, the angular coefficients are[30]

$$f_k(\underline{\ell},\ell';L) = (-)^L\langle\ell\,\|\,C^{(k)}\,\|\,\ell\rangle\langle\ell'\,\|\,C^{(k)}\,\|\,\ell'\rangle\begin{Bmatrix}\ell & \ell' & L\\ \ell' & \ell & k\end{Bmatrix}, \tag{17}$$

$$g_k(\underline{\ell},\ell';LS) = \frac{1}{2}\langle\ell\,\|\,C^{(k)}\,\|\,\ell'\rangle^2\left[-\frac{1}{[\ell,\ell']} + \delta_{L,k}\delta_{S,0}\frac{1}{[L]}\right], \tag{18}$$

where the reduced-matrix element is defined as

$$\langle\ell\,\|\,C^{(k)}\,\|\,\ell'\rangle \equiv (-)^\ell[\ell,\ell']^{1/2}\begin{pmatrix}\ell & k & \ell'\\ 0 & 0 & 0\end{pmatrix}, \tag{19}$$

with shorthand $[\ell,\ell'] \equiv (2\ell+1)(\ell'+1)$. The allowed k values follow from the triangle conditions of the $3j$ and $6j$ symbols. The coefficients $f_k(\ell,\ell')$ are nonzero for $k = 0,2,\ldots,$ $\min(2\ell,2\ell')$. The coefficients $g_k(\ell,\ell')$ with $n\ell \neq n'\ell'$ are nonzero for $k = |\ell-\ell'|,|\ell-\ell'+2|,\ldots,\ell+\ell'$.

The values of f_k and g_k obtained for d^9f^1 are given in Table II. Since the Coulomb interaction has no spin dependence, $f_k(\underline{\ell},\ell;L)$ has the same value for singlet and triplet states. The coefficient $g_k(\underline{\ell},\ell;LS)$ has the same value for all LS states, except for singlet states with $L = k$ (boldfaced numbers in Table II).

The Slater integrals F^k and G^k can be regarded as adjustable physical parameters. Their values obtained by Hartree-Fock (HF) calculations[25] are given in Table III. They are usually scaled to 70%–80% to take into account configuration interaction and screening.[20,26,31]

The last column in Table II gives the final-state energies for U $5d^95f^1$ using the corresponding Slater parameters from Table III scaled to 70% and without spin-orbit interaction. The ^1P state has much higher energy than the other LS states, which is due to the extra term $\delta_{L,k}\delta_{S,0}[L]^{-1}$ in Eq. (18). The exchange integral $G^1(5d,5f)$ gives a large contribution to the energy of the ^1P state and contributes only little to the energy of the other

TABLE III. Calculated Hartree-Fock values (in eV) of the Slater parameters F^k and G^k (before scaling) and spin-orbit parameters ζ_ℓ for different $d^9 f^1$ configurations.

	U $5d^9 5f^1$ $O_{4,5}$	U $4d^9 5f^1$ $N_{4,5}$	La $4d^9 4f^1$ $N_{4,5}$	La $3d^9 4f^1$ $M_{4,5}$
F^0	103.3	766.3	103.4	841.7
$F^2(d,f)$	11.575	5.730	13.067	7.063
$F^4(d,f)$	7.547	2.350	8.325	3.167
$G^1(d,f)$	13.845	1.027	15.523	4.723
$G^3(d,f)$	8.620	1.112	9.669	2.761
$G^5(d,f)$	6.175	0.914	6.817	1.905
ζ_d	3.282	17.412	1.117	6.799
ζ_f	0.323	0.344	0.077	0.092
$G^1(d,f)/\zeta_d$	4.21	0.059	13.9	0.695

LS states (cf. Table II). The values of $G^1(d,f)$ in Table III show that this effect is very strong for the $nd \to nf$ transitions, but much smaller for the $(n-1)d \to nf$ transitions in the actinides and rare earths. The physical reason is that the orbital planes of the d^9 and f^1 electronic charge clouds coincide in the ^1P state, which results in a high repulsive energy when both shells have the same principal quantum number n. Due to the higher multipolarity, the G^3 and G^5 integrals give relatively lower contributions to the exchange energies of the $^1F_3$ and $^1H_5$ states, respectively, so that their energies in the $k = 3$ and 5 spectra are not especially large.

C. Comparison with final state $d^9 f^{13}$

It is instructive to compare the electrostatic interaction for $d^9 f^1$ (one hole and one electron) with $d^9 f^{13}$ (two holes). While the Coulomb coefficients have opposite sign, $f_k(\underline{\ell},\underline{\ell}';L) = f_k(\ell,\ell';L) = -f_k(\underline{\ell},\ell';L)$, the coefficients $g_k(\underline{\ell},\underline{\ell}';LS)$ and $g_k(\underline{\ell},\ell';LS)$ are rather different. Instead of Eq. (18), we have[30]

$$g_k(\underline{\ell},\underline{\ell}';LS) = \langle \ell \,\|\, C^{(k)} \,\|\, \ell' \rangle^2 \left[\frac{1}{2[\ell,\ell']} + (-)^S \begin{Bmatrix} \ell & \ell' & L \\ \ell & \ell' & k \end{Bmatrix} \right]. \tag{20}$$

The values of f_k and g_k for $d^9 f^{13}$ are given in Table IV, which can be compared with $d^9 f^1$ in Table II. The exchange interaction G^1 contributes differently to each LS state and is largest between $^1H_5$ and $^3H_5$. The ^1P state in $d^9 f^{13}$ has no longer an exceptionally high energy. Thus, the exchange integral leads to a different result in the light and heavy elements of the series.

TABLE IV. Values of the coefficients f_k and g_k for $d^9 f^{13}$ using Eqs. (17) and (20). The last column gives the final-state energies (in eV) using the same Slater parameters as used for U $5d^9 5f^1$ in Table II.

	f_2	f_4	g_1	g_3	g_5	$E(N_{4,5})$
$^3P_1$	8/35	2/21	1/70	−2/35	−15/77	1.31
$^3H_5$	2/21	1/231	−27/70	−4/315	160/7623	−2.92
$^3D_{1,3}$	2/35	−1/7	9/70	16/105	−20/231	1.50
$^3F_3$	−11/105	2/21	−9/70	−13/315	−10/693	−1.90
$^1H_5$	2/21	1/231	33/70	16/315	170/7623	5.77
$^3G_{3,5}$	−1/7	−2/63	23/70	−29/315	10/693	1.37
$^1F_3$	−11/105	2/21	3/14	5/63	40/693	2.46
$^1P_1$	8/35	2/21	1/14	2/21	−5/21	4.65

D. Spin-orbit interaction

The Hamiltonian of the spin-orbit interaction for an electron in the ℓ shell is $H = \zeta_\ell(r)\, \ell \cdot s$, where $\zeta_\ell(r)$ is the radial part and $\ell \cdot s$ the angular part. The angular part is equal to $-\frac{1}{2}(\ell+1)$ and $\frac{1}{2}\ell$ for $j = \ell - \frac{1}{2}$ and $j = \ell + \frac{1}{2}$, respectively. Thus, the energies of the levels for $d^9 f^1$ are

$$\begin{aligned} E(\underline{d}_{3/2} f_{7/2}) &= 3/2\zeta_d + 3/2\zeta_f = 5.408 \text{ eV}, \\ E(\underline{d}_{3/2} f_{5/2}) &= 3/2\zeta_d - 2\zeta_f = 4.277 \text{ eV}, \\ E(\underline{d}_{5/2} f_{7/2}) &= -\zeta_d + 3/2\zeta_f = -2.798 \text{ eV}, \\ E(\underline{d}_{5/2} f_{5/2}) &= -\zeta_d - 2\zeta_f = -3.928 \text{ eV}, \end{aligned} \tag{21}$$

where the values in the last column have been obtained by substituting $\zeta_d = 3.282$ eV and $\zeta_f = 0.323$ eV for the U $N_{4,5}$ edge (cf. Table III). The spin-orbit interaction is diagonal in the jj basis. However, in intermediate coupling, the final-state Hamiltonian is more conveniently expressed using LS basis states. Hence, this requires transformation matrices between jj and LS basis states.

E. $jj \leftrightarrow LS$ transformation

The Hamiltonian in spherical symmetry is block-diagonal in J, which is a good quantum number. For each J block, the LS- and jj-coupled basis states are transformed using recoupling coefficients, which are expressed in $9j$ symbols,

$$\begin{aligned} &\langle \psi\{[(\ell,\ell')L,(s,s')S]J\} \mid \psi\{[(\ell,s)j,(\ell',s')j']J\}\rangle \\ &\quad = [L,S,j,j']^{1/2} \begin{Bmatrix} \ell & \ell' & L \\ s & s' & S \\ j & j' & J \end{Bmatrix}, \end{aligned} \tag{22}$$

where $[L,S,\ldots] \equiv (2L+1)(2S+1)\ldots$. The coefficients give for each J block a transformation matrix $\mathbf{T} = \langle \psi(LS) | \psi(jj)\rangle$, which is an orthogonal matrix, meaning a square matrix whose transpose is also its inverse. The matrices transform the wave functions and operators as

$$\psi(jj) = \mathbf{T} \cdot \psi(LS), \tag{23a}$$

$$O_{(jj)} = \mathbf{T} \cdot O_{(LS)} \cdot \mathbf{T}^{-1}, \tag{23b}$$

respectively. For our purpose, we need the matrices with $J = k$ for the allowed k values.

For $k = 1$, the matrix with $J = 1$ for a transformation $\psi(d_{3/2}f_{5/2}, d_{5/2}f_{7/2}, d_{5/2}f_{5/2}) = \mathbf{T}^{(1)} \cdot \psi(^3D_1, ^3P_1, ^1P_1)$ is

$$\mathbf{T}^{(1)} = \begin{pmatrix} \sqrt{\frac{2}{5}} & \sqrt{\frac{1}{5}} & \sqrt{\frac{2}{5}} \\ -\sqrt{\frac{1}{7}} & -\sqrt{\frac{2}{7}} & \sqrt{\frac{4}{7}} \\ -\sqrt{\frac{16}{35}} & \sqrt{\frac{18}{35}} & -\sqrt{\frac{1}{35}} \end{pmatrix}. \tag{24}$$

For $k = 3$, the matrix with $J = 3$ for a transformation $\psi(d_{3/2}f_{7/2}, d_{3/2}f_{5/2}, d_{5/2}f_{7/2}, d_{5/2}f_{5/2}) =$

$\mathbf{T}^{(3)} \cdot \psi(^3G_3, ^3F_3, ^3D_3, ^1F_3)$ is

$$\mathbf{T}^{(3)} = \begin{pmatrix} \frac{1}{7}\sqrt{3} & \sqrt{\frac{3}{7}} & \frac{3}{7}\sqrt{2} & -\frac{1}{\sqrt{7}} \\ \frac{3}{14}\sqrt{15} & \frac{1}{2}\sqrt{\frac{3}{35}} & -\frac{2}{7}\sqrt{\frac{2}{5}} & \frac{3}{\sqrt{35}} \\ -\frac{3}{14} & -\frac{1}{2\sqrt{7}} & \frac{2}{7}\sqrt{6} & \sqrt{\frac{3}{7}} \\ -\frac{1}{7}\sqrt{10} & 3\sqrt{\frac{2}{35}} & -\frac{3}{7}\sqrt{\frac{3}{5}} & \sqrt{\frac{6}{35}} \end{pmatrix}. \quad (25)$$

For $k = 5$, the matrix with $J = 5$ for a transformation $\psi(d_{3/2}f_{7/2}, d_{5/2}f_{7/2}, d_{5/2}f_{5/2}) = \mathbf{T}^{(5)} \cdot \psi(^3H_5, ^3G_5, ^1H_5)$ is

$$\mathbf{T}^{(5)} = \begin{pmatrix} \frac{2}{5}\sqrt{3} & \frac{1}{5}\sqrt{3} & -\sqrt{\frac{2}{5}} \\ -\frac{1}{5\sqrt{7}} & \frac{12}{5\sqrt{7}} & \sqrt{\frac{6}{35}} \\ 3\sqrt{\frac{2}{35}} & -\sqrt{\frac{2}{35}} & \sqrt{\frac{3}{7}} \end{pmatrix}. \quad (26)$$

F. Transition probabilities of $j_d j_f$ states

It is instructive at this point to determine the intensities of the jj-coupled final states, which need no matrix diagonalization. Using the transformation matrix $\mathbf{T}^{(1)}$, the jj-coupled wave functions with $J = 1$ are obtained as LS-coupled wave functions

$$\begin{aligned} \psi(d_{3/2}f_{5/2}) &= \sqrt{\frac{2}{5}}\psi(^3D) + \sqrt{\frac{1}{5}}\psi(^3P) + \sqrt{\frac{2}{5}}\psi(^1P), \\ \psi(d_{5/2}f_{7/2}) &= -\sqrt{\frac{1}{7}}\psi(^3D) - \sqrt{\frac{2}{7}}\psi(^3P) + \sqrt{\frac{4}{7}}\psi(^1P), \quad (27) \\ \psi(d_{5/2}f_{5/2}) &= -\frac{4}{\sqrt{35}}\psi(^3D) + \frac{6}{\sqrt{70}}\psi(^3P) + \frac{1}{\sqrt{35}}\psi(^1P). \end{aligned}$$

Electric-dipole transitions are only allowed to states with $^1P_1$ character, thus the transition probability to the $j_d j_f$ state is given by $|\langle\psi(j_d j_f)|\psi(^1P_1)\rangle|^2$, which is the square of the wave-function coefficient. The $k = 3$ and 5 transitions are only allowed to states with $^1F_3$ and $^1H_5$ character, respectively, and their transition probabilities are derived in the same manner. The resulting intensities for the pure $j_d j_f$ states are listed in Table V. It might seem remarkable that each 2^k-pole transition has a ratio of the summed intensities equal to $\sum I(d_{3/2}):\sum I(d_{5/2}) = 2/5 : 3/5$ and $\sum I(f_{5/2}):\sum I(f_{7/2}) = 3/7 : 4/7$, which corresponds precisely to the statistical ratio of these j levels. However, this is simply a consequence of the spin-orbit sum rule for electric-multipole transitions.[7] Due the absence of spin-orbit interaction in the initial state $^1S_0$, the spin-orbit-split levels in the final state have a statistical intensity ratio (see also Sec. IV B).

TABLE V. Multipole intensities for the pure $j_d j_f$ levels in the $f^0 \to d^9 f^1$ transition. Each multipole transition gives $\sum I(d_{3/2}):\sum I(d_{5/2}) = 2/5 : 3/5$ and $\sum I(f_{5/2}):\sum I(f_{7/2}) = 3/7 : 4/7$.

	$I(d_{3/2}f_{7/2})$	$I(d_{3/2}f_{5/2})$	$I(d_{5/2}f_{7/2})$	$I(d_{5/2}f_{5/2})$
$k = 1$	0	2/5	4/7	1/35
$k = 3$	1/7	9/35	3/7	6/35
$k = 5$	2/5	0	6/35	3/7

G. Final-state Hamiltonian

The next step is to compose the final-state Hamiltonians for the various multipole transitions. To put electrostatic interactions and spin-orbit coupling on equal footing requires intermediate coupling, which can be conveniently expressed in LS basis states. The Hamiltonian in jj coupling with the diagonal spin-orbit elements given in Eq. (21) is transformed using Eqs. (24)–(26) to LS coupling, in which scheme the diagonal electrostatic terms can be included. The resulting final-state Hamiltonians for $k = 1$, 3, and 5 are given in Eqs. (28)–(30), where the choice of LS basis set is clear from the LS energy terms along the diagonal:

$$\mathcal{H}^{(1)}_{(LS)} = \begin{pmatrix} E(^3D) - \frac{3}{2}\zeta_f & \frac{1}{2}\sqrt{2}(\zeta_d + \zeta_f) & \zeta_d - \zeta_f \\ \frac{1}{2}\sqrt{2}(\zeta_d + \zeta_f) & E(^3P) - \frac{1}{2}\zeta_d - \zeta_f & \frac{1}{2}\sqrt{2}(\zeta_d + 2\zeta_f) \\ \zeta_d - \zeta_f & \frac{1}{2}\sqrt{2}(\zeta_d + 2\zeta_f) & E(^1P) \end{pmatrix}, \quad (28)$$

$$\mathcal{H}^{(3)}_{(LS)} = \begin{pmatrix} E(^3G) + \frac{1}{8}(7\zeta_d - 13\zeta_f) & \frac{15}{56}\sqrt{7}(\zeta_d + \zeta_f) & 0 & \frac{5}{4}\sqrt{\frac{3}{7}}(\zeta_d - \zeta_f) \\ \frac{15}{56}\sqrt{7}(\zeta_d + \zeta_f) & E(^3F) + \frac{1}{8}(\zeta_d - 3\zeta_f) & \sqrt{\frac{6}{7}}(\zeta_d + \zeta_f) & -\frac{1}{4}\sqrt{3}(\zeta_d + 3\zeta_f) \\ 0 & \sqrt{\frac{6}{7}}(\zeta_d + \zeta_f) & E(^3D) + \zeta_f & -\frac{3}{14}\sqrt{14}(\zeta_d - \zeta_f) \\ \frac{5}{4}\sqrt{\frac{3}{7}}(\zeta_d - \zeta_f) & -\frac{1}{4}\sqrt{3}(\zeta_d + 3\zeta_f) & -\frac{3}{14}\sqrt{14}(\zeta_d - \zeta_f) & E(^1F) \end{pmatrix}, \quad (29)$$

$$\mathcal{H}^{(5)}_{(LS)} = \begin{pmatrix} E(^3H) - \frac{1}{10}(2\zeta_d - 3\zeta_f) & \frac{3}{5}(\zeta_d + \zeta_f) & -\sqrt{\frac{3}{10}}(2\zeta_d + 3\zeta_f) \\ \frac{3}{5}(\zeta_d + \zeta_f) & E(^3G) - \frac{1}{10}(7\zeta_d - 13\zeta_f) & -\frac{3}{10}(\zeta_d - \zeta_f) \\ -\sqrt{\frac{3}{10}}(2\zeta_d + 3\zeta_f) & -\frac{3}{10}(\zeta_d - \zeta_f) & E(^1H) \end{pmatrix}. \quad (30)$$

For the uranium $O_{4,5}$ edge, the energy splitting of the spin-orbit interaction is $\frac{5}{2}\zeta_d \approx 8.2$ eV. This can be compared with the largest energy separation due to the electrostatic interaction in $d^9 f^1$ (cf. Table II), which is

$$\begin{aligned} E(^3D) - E(^1P) &= 16.74 \text{ eV for } k = 1, \\ E(^1F) - E(^3D) &= 2.35 \text{ eV for } k = 3, \\ E(^3G) - E(^3H) &= 2.12 \text{ eV for } k = 5. \end{aligned} \tag{31}$$

Thus, while the $k = 1$ spectrum is closer to LS coupling, the $k = 3$ and 5 spectra, on the other hand, are closer to jj coupling, which has profound implications for the spectral analysis.

H. First-moment sum rule

As explained in Sec. III F, electric-multipole transitions of rank $k = 1$, 3, and 5 are allowed to states with $^1P_1$, $^1F_3$, and $^1H_5$ character, respectively. We will indicate these terms generically as ^1K_k. For the $f^0 \to d^9 f^1$ transition, we can formulate a useful sum rule relating the first moment of the k spectrum to the energy of the ^1K_k state.

For each multipole rank k, the eigenvalues E_i^k and eigenstates ψ_i^k (with running index i) are obtained by diagonalizing the Hamiltonian $\mathcal{H}_{(LS)}^{(k)}$. The intensities of the final states ψ_i^k are given by the square of the wave-function coefficients

$$I_i^k = \left|\langle \psi_i^k | \psi(^1K_k)\rangle\right|^2. \tag{32}$$

The energy term $E(^1K_k)$ is a diagonal matrix element in the LS-coupled Hamiltonian, and because the trace of the matrix is conserved, the average energy of the k spectrum is

$$\frac{\sum_i I_i^k E_i^k}{\sum_i I_i^k} = E(^1K_k) \equiv g E(^1K_k)_{\rm HF}. \tag{33}$$

Thus, the first moment of the spectrum (i.e., the sum over the normalized intensities I_i^k times their energy E_i^k) is equal to the HF energy $E(^1K_k)_{\rm HF}$ of the ^1K_k state with scaling factor g for the Slater integrals. Note that the HF energies have been corrected for the spherically averaged electrostatic energy in Eq. (16). This sum rule shows that the average energy does not depend on the final-state spin-orbit interaction, as will be illustrated by the example in Fig. 1 described in the following section. General expressions for spectral moment distributions can be found in Ref. 32.

I. Interplay between spin-orbit and electrostatic interactions

Figure 1 shows the uranium $5f^0 \to 5d^9 5f^1$ multipole spectra calculated for different scaling factors g of the Slater parameters and z of the spin-orbit parameter. Figure 1(a) shows the energy positions of the LS levels in the absence of spin-orbit interaction (values in the last column of Table II). The electrostatic interaction gives an energy spread over the LS states of several eV, except for the ^1P, which has much higher energy for reasons explained in Sec. III B. Figure 1(b) shows the peaks allowed in LS coupling, i.e., $^1P_1$, $^1F_3$, and $^1H_5$ for $k = 1$, 3, and 5, respectively.

Switching on the spin-orbit interaction in Fig. 1(c) mixes the singlet with the triplet states, listed in Table I. For $k = 1$, the $^3P_1$ and $^3D_1$ become allowed, however, their intensity remains low because the mixing with the remote $^1P_1$ is small. Since the dipole-allowed pure $^1P_1$ state has exceptionally high energy, the intensity of the $k = 1$ spectrum is at a very high energy compared to the average energy of the final-state configuration. The $^1P_1$ state is pushed up further in energy in the presence of spin-orbit interaction [cf. Figs. 1(b) and 1(c)]. Note that the energy positions of the peaks obey the sum rule in Eq. (33), so that the average energy of the spectrum remains the same for constant g. Reducing the electrostatic interactions (from $g = 0.7$ to 0.3) in Fig. 1(d) shifts the $^1P_1$ to lower energy.

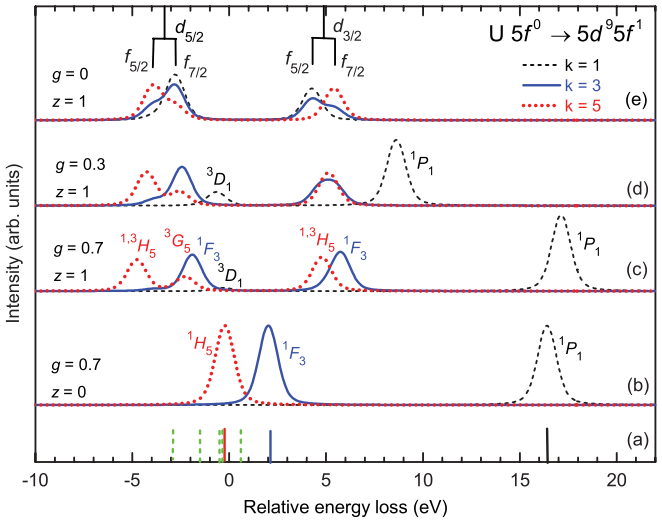

FIG. 1. (Color online) Uranium $O_{4,5}$ NIXS. Calculated multipole spectra with $k = 1$ (dashed black line), $k = 3$ (drawn blue line), and $k = 5$ (dotted red line) for the transitions U $5f^0 \to 5d^9 5f^1$, varying the scaling factors g for the Slater parameter and z for the spin-orbit parameter. (a) Energy positions of the LS states for $g = 0.7$, $z = 0$ (values in last column of Table II). Nonallowed states are dashed. NIXS spectra for (b) only electrostatic interactions; $g = 0.7$, $z = 0$ (LS-coupling limit), (c) realistic values: $g = 0.7$, $z = 1$ (intermediate coupling scheme applies), (d) strongly reduced electrostatic interactions: $g = 0.3$, $z = 1$, and (e) only spin-orbit interaction: $g = 0$, $z = 1$ (jj-coupling limit) with assignment $j_d j_f$. For the $J = 0$ ground state, the 2^k-pole transitions are only allowed to final states with $J = k$. For relatively pure peaks, the approximate peak assignment is indicated. The calculated spectra have been convoluted with a Lorentzian of $\Gamma = 0.2$ eV and Gaussian of $\sigma = 0.4$ eV.

The situation is completely different for $k = 3$ and 5, where the energy difference between the allowed states is much smaller. Figure 1(e) shows the spectra without electrostatic interaction, where the spin-orbit interaction gives the four energy levels from Eq. (21). The average energy of each k spectrum is zero since $g = 0$ [cf. Eq. (33)]. The $5d$ spin-orbit interaction gives the large energy splitting and the $5f$ spin-orbit interaction gives the smaller splitting. The peak intensities for the various multipole spectra are given in Table V. In jj coupling, the peak intensities are independent of the energy positions, i.e., they do not depend on the size of the spin-orbit splitting. This also follows from the spin-orbit sum rule.[7] It is seen that the scaling of the electrostatic interaction has a much smaller influence on the $k = 3$ and 5 spectra.

The higher k spectra show a clear energy separation between the $5d_{5/2}$ and $5d_{3/2}$ structures, arising from the dominant spin-orbit interaction. Changes due to the electrostatic interaction are larger in the $5d_{3/2}$ structure because the $k = 5$ peak in jj coupling is at higher energy, while it is at lower energy in LS coupling. This means that at some stage the $k = 5$ and 3 peaks have to cross each other, which occurs around $g = 0.3$ and $z = 1$. In the $5d_{5/2}$ structure, on the other hand, the $k = 5$ is always at lower energy than the $k = 3$ peak. Thus, while the $5d_{3/2}$ feature is narrow, the $5d_{5/2}$ remains a distinct doublet. In this way, the $5d_{3/2}$ structure of the $5f^0$ NIXS can give an estimation of the scaling factor g for the electrostatic interaction.

IV. ACTINIDE $O_{4,5}$ SPECTRA

We present here the calculated multipole spectra at the $O_{4,5}$ edges from Th f^0 to Cf f^9 and discuss the systematic trends in these spectra. To gain a deeper understanding of the various peak structures, the spectra calculated in intermediate coupling are compared with those without $5d$ spin-orbit interaction (LS-coupling limit) and without $5f$-$5d$ electrostatic interactions (jj-coupling limit). The initial state is always in intermediate coupling in order to keep it the same for all three cases considered. The integrated intensity of each spectrum is formally proportional to the number of holes in the f shell, however, for better comparison, the k spectra for the different f^n configurations are plotted with equal normalized integrated intensity.

A. Final state without spin-orbit interaction

The final state is taken in the LS-coupling limit. From an initial state LSJ, the final-state levels $L'S'J'$ can be reached that have $|L - k| \leqslant L' \leqslant L + k$, $S' = S$, and $|J - k| \leqslant J' \leqslant J + k$, which can amount to a large number of final-state levels.

Higher L values have often lower energies, although this is not completely regular (see, e.g., Table II), which implies that higher multipole spectra have on average lower energies. The actinide spectra without $5d$ spin-orbit interaction are displayed in Fig. 2, showing that the accessible LS states for $k = 5$ are indeed lower in energy than for $k = 3$. For less than half-filled $5f$ shell, the states for $k = 1$ are much higher in energy, but from f^7 onwards they have shifted to lower energy. This energy shift caused by the exchange integral G^1 is thus manifest far beyond f^0.

B. Final state without electrostatic interaction

The final state is taken in the jj-coupling limit. The calculated actinide spectra without $5d$-$5f$ electrostatic interaction are shown in Fig. 3. The $5d$ spin-orbit interaction gives a neat splitting into two edges, where each edge shows a small energy spread over the various final-state J levels. A powerful tool to analyze core-level spectra, in which j is a good quantum number, is provided by the branching ratio,[33] which is defined for each k spectrum as the integrated intensity ratio of the $5d$

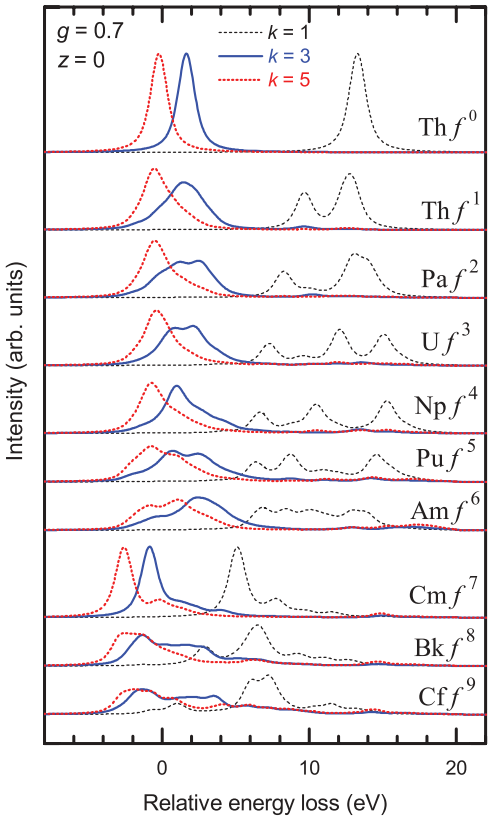

FIG. 2. (Color online) Actinide $O_{4,5}$ multipole spectra without $5d$ spin-orbit interaction ($g = 0.7$, $z = 0$), showing the calculations with $k = 1$ (dashed black line), $k = 3$ (drawn blue line), and $k = 5$ (dotted red line) for the transitions $5f^n \rightarrow 5d^9 5f^{n+1}$. The line spectra were convoluted with a Lorentzian of $\Gamma = 0.5$ eV and Gaussian of $\sigma = 0.3$ eV.

spin-orbit split levels,

$$B^k \equiv \frac{\int I^k(d_{5/2})dE}{\int I^k(d_{5/2})dE + \int I^k(d_{3/2})dE}. \tag{34}$$

According to the spin-orbit sum rule, the branching ratio B^k is proportional to w_h, which is the angular part of the $5f$ spin-orbit interaction per hole.[7] For the $d \rightarrow f$ transition, this sum rule gives

$$B^1 = \tfrac{3}{5} + \tfrac{2}{5}w_h, \tag{35a}$$

$$B^3 = \tfrac{3}{5} + \tfrac{3}{20}w_h, \tag{35b}$$

$$B^5 = \tfrac{3}{5} - \tfrac{3}{10}w_h, \tag{35c}$$

where

$$w_h \equiv -\frac{1}{\ell s h}\sum_{i=1}^{h} \ell_i \cdot s_i = \frac{1}{h}\left(-\frac{\ell+1}{\ell}h_{f5/2} + h_{f7/2}\right), \tag{36}$$

with $h = h_{f5/2} + h_{f7/2}$ the total number of f holes in the initial state, and $h_{f5/2}$ and $h_{f7/2}$ the number of $f_{5/2}$ and $f_{7/2}$ holes, respectively.

Calculated values of w_h for the actinides can be found in Ref. 34. The absence of $5f$ spin-orbit interaction in Th f^0 gives that all its k spectra have a branching ratio equal to the

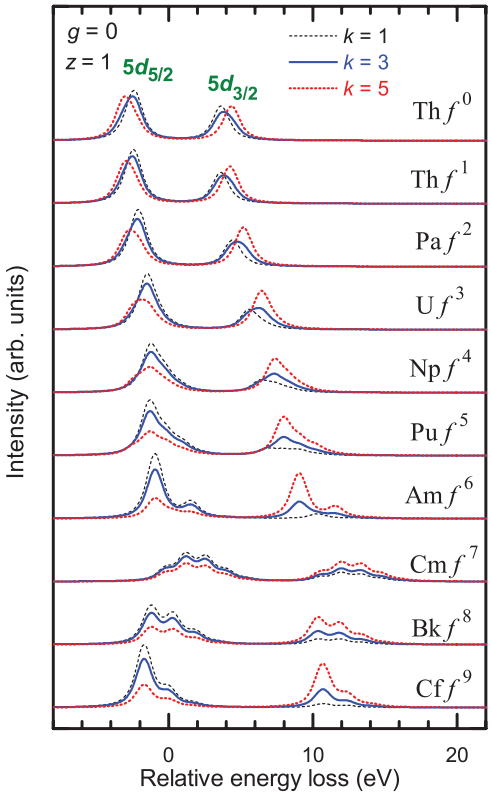

FIG. 3. (Color online) Actinide $O_{4,5}$ multipole spectra without $5d$-$5f$ electrostatic interactions ($g = 0$, $z = 1$), showing calculations with $k = 1$ (dashed black line), $k = 3$ (drawn blue line), and $k = 5$ (dotted red line) for the transitions $5f^n \rightarrow 5d^9 5f^{n+1}$. The line spectra were convoluted with a Lorentzian of $\Gamma = 0.5$ eV and Gaussian of $\sigma = 0.3$ eV.

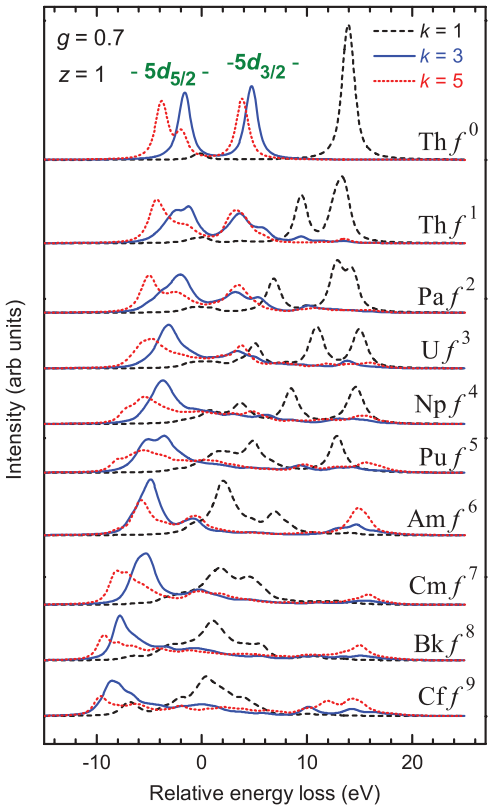

FIG. 4. (Color online) Actinide $O_{4,5}$ NIXS in intermediate coupling. Calculated multipole spectra with $k = 1$ (dashed black line), $k = 3$ (drawn blue line), and $k = 5$ (dotted red line) for the transitions $5f^n \rightarrow 5d^9 5f^{n+1}$. The scaling factor for the Slater parameters is $g = 0.7$. The line spectra were convoluted with a Lorentzian of $\Gamma = 0.5$ eV and Gaussian of $\sigma = 0.3$ eV.

statistical ratio of $3/5$. The hole states in the f^n shell prefer a parallel coupling of ℓ and s, giving a ground state with negative spin-orbit energy and hence positive w_h. Thus, according to Eq. (35), for the ground state the branching ratio is higher for $k = 1$ than for $k = 3$, which on its turn is higher than for $k = 5$. Equation (36) shows that the value of w_h increases for decreasing the number of holes h. Therefore, the differences in B^1, B^3, and B^5 become larger for heavier elements, as can be verified by inspecting the spectra in Fig. 3.

C. Final state in intermediate coupling

The $O_{4,5}$ multipole spectra calculated in intermediate coupling are shown in Fig. 4. It is seen that for the dipole spectra the calculations in intermediate coupling are quite similar to those in the LS-coupling limit, shown in Fig. 2, with Am f^6 as the main exception. The dramatic energy shift in the dipole spectrum between Pu f^5 and Am f^6 is confirmed by the experimental EELS spectra (Fig. 12 in Ref. 8). Overall, the LS-coupling limit is a reasonable approximation for the dipole spectrum. In fact, the large exchange integral G^1 makes LS coupling a good approximation for the lighter elements. Furthermore, as first pointed out by Sugar,[31] the interaction G^1 preserves the $d^9 f^1$ parentage, from which we may infer that LS coupling is appropriate for dipole spectra up to halfway the series.

In the $k = 3$ and 5 spectra, the $5d$ spin-orbit splitting, which plays such a prominent role in $5f^0$, clearly keeps up its appearance till f^3, while in the $5d_{3/2}$ region the intensity gradually diminishes. For higher f counts, these spectra regain intensity at high photon energies.

Figure 4 shows that for heavier elements, the overall peak intensity in the low-energy region is smaller for $k = 5$ than for $k = 3$, with the opposite in the high-energy region ($\sim$15 eV in Pu-Cf). This intensity balance is a consequence of the spin-orbit sum rule, fueled by the prominence of the $5d$ spin-orbit splitting. In other words, the low-energy states have predominantly $5d_{5/2}$ core-hole character, whereas the high-energy states have more $5d_{3/2}$ character.

The dipole spectrum splits into several peaks, which for the lighter elements coincide with the giant resonance, as can be seen from, e.g., the experimental EELS spectra (Fig. 12 in Ref. 8). The calculations do not include any decay channels which cause the Fano broadening in the high-energy region.[35,36] The high-energy states of the experimental dipole spectrum are broadened because their energy coincides with interacting continuum states. The lifetime broadening of the different LS states can vary strongly depending on the availability of LS states to which decay is allowed.[37,38] This means for Th f^0 that while the $^1P_1$ peak is broad, the $^3P_1$ and $^3D_1$ prepeaks are much narrower. However, going more towards the jj-coupling limit, the LS states will strongly mix,

so that all peaks obtain a similar lifetime broadening, which would occur in the higher multipole spectra.

D. Comparison to experimental data

Figure 5 shows a comparison of the calculated spectra for U $5f^1$, $5f^2$, and $5f^3$ with the experimental $O_{4,5}$ NIXS spectra of UO_2 measured at $q = 1.68$ and 9.74 Å^{-1}.[5] At low q, the NIXS spectrum is dominated by dipole transitions, whereas at high q the NIXS spectrum consists mainly of octupole ($k = 3$) and triacontadipole ($k = 5$) transitions. Figure 5 shows the calculated NIXS as simulated spectra with an intensity ratio of $I^5/I^3 = 1.18$, which is the ratio expected for $q = 9.74$ Å^{-1} derived by using the Bessel functions in Eq. (7).[5]

The high-q spectra clearly show a pronounced splitting due to the $5d$ spin-orbit interaction with the electrostatic interaction giving detailed structure at each edge. The multiplet structure due to the electrostatic interaction is partly resolved for the higher multipole spectra of the actinide $O_{4,5}$, despite the relatively large core-level width of $\Gamma = 0.5$ eV. It is the electrostatic interaction that gives rise to the characteristic multiplet structure, such as for the localized $3d$ transition-metal $L_{2,3}$ XAS,[24,39] and rare-earth $M_{4,5}$ XAS.[26] In other cases, such as for the actinide $N_{4,5}$ and $M_{4,5}$ XAS, the multiplet structure disappears in the linewidth broadening.

The best agreement with the NIXS from UO_2 is obtained for U f^2 in Fig. 5. For uranium it might seem that the dependence on the valence state (or element specificity) is modest. However, there are some quite remarkable changes across the actinide series. The $k = 3$ spectrum from Pu f^5 in Fig. 4 shows a well-resolved doublet structure, whereas the same k spectra from the adjacent f^4 and f^6 elements have only a single peak.

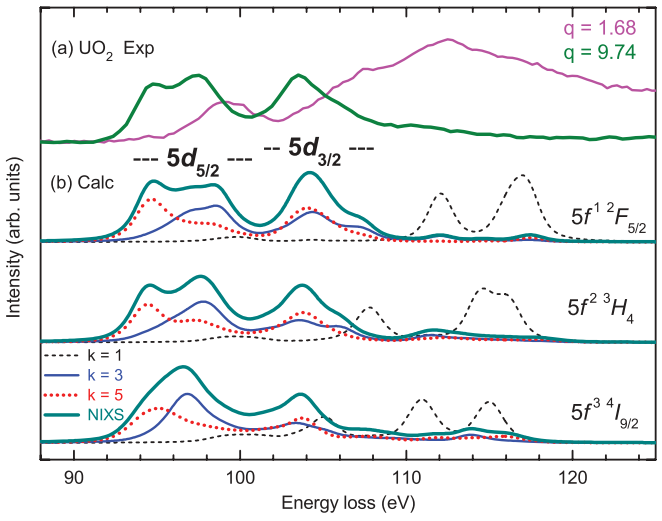

FIG. 5. (Color online) Uranium $O_{4,5}$ NIXS. (a) Experimental spectra of UO_2 for $q = 1.68$ Å^{-1} (drawn olive line) and $q = 9.74$ Å^{-1} (drawn magenta line) from Ref. 5. (b) Calculated multipole spectra I^k with $k = 1$ (dashed black line), $k = 3$ (drawn blue line), and $k = 5$ (dotted red line) for Hund's rule ground state U $5f^1$, $5f^2$, and $5f^3$ with scaling factor $g = 0.7$ for the Slater parameters. The calculated spectra were convoluted with a Lorentzian of $\Gamma = 0.5$ eV and Gaussian of $\sigma = 0.5$ eV. The simulated NIXS spectrum (thick dark cyan line) is equal to $1.18\,I^5 + I^3$.

V. RARE-EARTH $N_{4,5}$ SPECTRA

Measurements for rare earths show a strong $N_{4,5}$ NIXS, in excellent agreement with the calculated multiplet structure.[6,40] The spectra for Ce $4f^1$, Pr $4f^2$, and Nd $4f^3$ can be found elsewhere.[6] Here, we will present only some results that serve as a comparison with the actinide $O_{4,5}$ NIXS.

Since the treatment of the $d \rightarrow f$ transition in Sec. III is completely general, it can be directly applied to La f^0 by using the appropriate physical parameters for the radial part of the spin-orbit interaction ζ_ℓ and the Slater integrals F^k and G^k (cf. Table III). The electrostatic interaction is more important in the rare-earth $N_{4,5}$ than in the actinide $O_{4,5}$ edge since ζ_d is larger in the latter. Figure 6 shows the $N_{4,5}$ spectra for the La $4f^0 \rightarrow 4d^9 4f^1$ transition. The intrinsic linewidth for the rare earths is expected to be narrower than for the actinides. Evidence for this arises from the experimental XAS and EELS spectra,[8,16,27] where $\Gamma \approx 0.1$ eV in the pre-edge structure. The linewidth does not directly depend on the rank of the multipole transition, although it depends on the particular LS states.

In the La $4f^0$ dipole spectrum, the purity of the final state is very high (99.7% for the $^1P_1$ and 96% for the $^3P_1$ and $^3D_1$ states). However, this is not the case in the $k = 3$ and 5 spectra, where the spin-orbit splitting ($\frac{5}{2}\zeta_d \approx 2.8$ eV) is of the same order as the electrostatic splitting in the allowed states. It is seen in Fig. 6 that the scaling factor g gives a strong energy shift of the $^1P_1$ peak in the dipole spectrum, but a much smaller shift of the peaks in the $k = 3$ and 5 spectra. This shift is of course governed by the final-state energy sum rule in Eq. (33).

Finally, we demonstrate the strong dependence on the initial-state angular momentum. Figure 7 shows a comparison between the multipole spectra of Ce $4f^1$ for the $J = 5/2$ Hund's rule ground state and the $J = 7/2$ state. For all k spectra, the pre-edge structure is very different between $J = 5/2$ and $7/2$ and provides a unique fingerprint. Note that the dipole spectrum has been multiplied by a factor 100

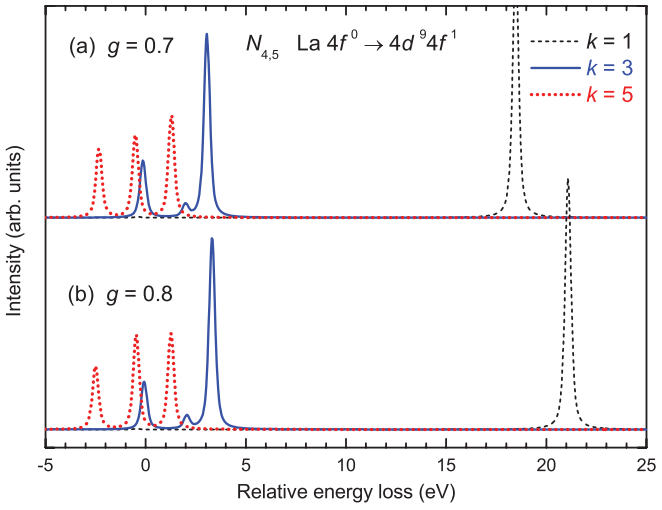

FIG. 6. (Color online) La $N_{4,5}$ NIXS. Calculated multipole spectra with $k = 1$ (dashed black line), $k = 3$ (drawn blue line), and $k = 5$ (dotted red line) for the transitions La $4f^0 \rightarrow 4d^9 4f^1$. The scaling factor for the Slater parameters is (a) $g = 0.7$ and (b) $g = 0.8$. The calculated spectra have been convoluted with a Lorentzian of $\Gamma = 0.1$ eV and Gaussian of $\sigma = 0.1$ eV.

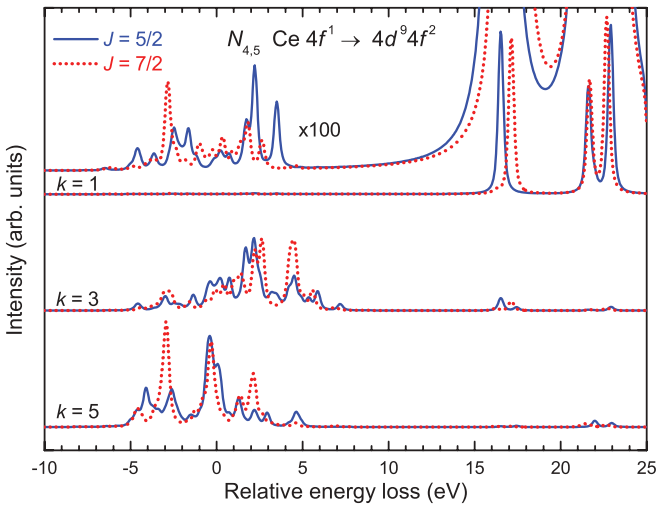

FIG. 7. (Color online) Cerium $N_{4,5}$ NIXS. Calculated multipole spectra with $k = 1$, $k = 3$, and $k = 5$ for the transition Ce $4f^1 \rightarrow 4d^9 4f^2$ with $J = 5/2$ (drawn blue line) and $J = 7/2$ (dotted red line). The scaling factor for the Slater parameters is $g = 0.8$. The calculated spectra have been convoluted with a Lorentzian of $\Gamma = 0.1$ eV and Gaussian of $\sigma = 0.1$ eV.

compared to the $k = 3$ and 5 spectra. Using high-resolution EELS, Bradley *et al.*[6] measured the detailed structure of the $k = 1$ pre-edge, which was shown to be in excellent agreement with the calculated multiplet structure.

VI. CONCLUSIONS

The $5d \rightarrow 5f$ multipole spectra of the actinide series represent a compelling case for investigating spectral structures. While the electric-dipole spectrum can be described rather well using LS coupling, for the higher multipole spectra, jj coupling is more appropriate. The exchange integral $G^1(5d,5f)$ pushes the ^1P state in $d^9 f^1$ to very high energy. From an initial state $^1S_0$ this is the only allowed state in LS coupling for the dipole spectrum. This spectrum is ~15 eV higher in energy than the configuration average, and the strong interaction with continuum states results in linewidth broadening.

In contrast to the dipole spectrum, in the higher multipole spectra the core spin-orbit splitting is larger than the electrostatic energy splitting. This leads to a spin-orbit-split doublet with a broad first peak and a narrower second peak. In the $5d_{5/2}$ region, the energy of the $k = 5$ peak is a few eV below that of the $k = 3$ peak. In the $5d_{3/2}$ region, the peaks are roughly at the same energy because spin-orbit and electrostatic interactions lead to opposite energy shifts.

The calculated NIXS spectra for the actinide series show large changes as a function of f count. This element or valence specificity will be useful in cases where the f count is under dispute, such as in δ-Pu metal or Pu oxides.[8,41]

For the $f^0 \rightarrow d^9 f^1$ transition, we gave a sum rule which relates the average energy of each k spectrum to the first moment of the spectral distribution. For this transition we also found that in jj coupling, the $j_d j_f$ levels have a fixed intensity ratio in the different k spectra, which finds its origin in the spin-orbit sum rule. According to this sum rule, the initial-state spin-orbit interaction per hole is linearly related to the core-level branching ratio. This leads to strong changes in the branching ratio of the $k = 3$ and 5 spectra, especially for heaver elements. For the ground state with lowest spin-orbit energy, higher k spectra have a lower branching ratio. Hence, in the low-energy region, the overall intensity of the $k = 3$ spectrum is higher than that of the $k = 5$ spectrum, whereas this is opposite in the high-energy region.

The rare-earth $4d \rightarrow 4f$ spectra for $k = 3$ and 5 exhibit a different behavior than the actinide $5d \rightarrow 5f$ spectra since the electrostatic and core spin-orbit splitting are comparable in size. However, the $k = 5$ peaks are still at lower energies than the $k = 3$ peaks. The calculated multipole spectra for different J levels show a strong variation in the pre-edge region.

The results of this study are expected to be very promising for performing NIXS measurements in a wide range of applications for actinides and rare-earth materials, such as under extreme conditions.

[1] W. Schülke, *Electron Dynamics by Inelastic X-Ray Scattering* (Oxford University Press, Oxford, UK, 2007).
[2] A. T. Macrander, P. A. Montano, D. L. Price, V. I. Kushnir, R. C. Blasdell, C. C. Kao, and B. R. Cooper, Phys. Rev. B **54**, 305 (1996).
[3] I. G. Gurtubay, J. M. Pitarke, W. Ku, A. G. Eguiluz, B. C. Larson, J. Tischler, P. Zschack, and K. D. Finkelstein, Phys. Rev. B **72**, 125117 (2005).
[4] B. C. Larson, J. Z. Tischler, W. Ku, C.-C. Lee, O. D. Restrepo, A. G. Eguiluz, P. Zschack, and K. D. Finkelstein, Phys. Rev. Lett. **99**, 026401 (2007).
[5] R. Caciuffo, G. van der Laan, L. Simonelli, T. Vitova, C. Mazzoli, M. A. Denecke, and G. H. Lander, Phys. Rev. B **81**, 195104 (2010).
[6] J. A. Bradley, K. T. Moore, G. van der Laan, J. P. Bradley, and R. A. Gordon, Phys. Rev. B **84**, 205105 (2011).
[7] G. van der Laan, Phys. Rev. Lett. **108**, 077401 (2012).
[8] K. T. Moore and G. van der Laan, Rev. Mod. Phys. **81**, 235 (2009).
[9] P. Santini, S. Carretta, G. Amoretti, R. Caciuffo, N. Magnani, and G. H. Lander, Rev. Mod. Phys. **81**, 807 (2009).
[10] R. G. Denning, J. C. Green, T. E. Hutchings, C. Dallera, A. Tagliaferri, K. Giarda, N. B. Brookes, and L. Braicovich, J. Chem. Phys. **117**, 8008 (2002).
[11] S. A. Kozimor, P. Yang, E. R. Batista, K. S. Boland, C. J. Burns, D. L. Clark, S. D. Conradson, R. L. Martin, M. P. Wilkerson, and L. E. Wolfsberg, J. Am. Chem. Soc. **131**, 12125 (2009).
[12] K. T. Moore, G. van der Laan, R. G. Haire, M. A. Wall, and A. J. Schwartz, Phys. Rev. B **73**, 033109 (2006).
[13] Y. F. Batrakov, A. G. Krivitsky, O. V. Pospelov, and E. V. Puchkova, Radiochim. Acta **92**, 73 (2004).
[14] G. Kalkowski, G. Kaindl, W. D. Brewer, and W. Krone, Phys. Rev. B **35**, 2667 (1987).
[15] T. Okane, Y. Takeda, J. Okamoto, K. Mamiya, T. Ohkochi, S.-I. Fujimori, Y. Saitoh, H. Yamagami, A. Fujimori, A. Ochiai *et al.*, J. Phys. Soc. Jpn. **77**, 024706 (2008).

[16]K. T. Moore and G. van der Laan, Ultramicroscopy **107**, 1201 (2007).
[17]J. A. Bradley, S. Sen Gupta, G. T. Seidler, K. T. Moore, M. W. Haverkort, G. A. Sawatzky, S. D. Conradson, D. L. Clark, S. A. Kozimor, and K. S. Boland, Phys. Rev. B **81**, 193104 (2010).
[18]M. Blume, J. Appl. Phys. **57**, 3615 (1985).
[19]J. A. Soininen, A. L. Ankudinov, and J. J. Rehr, Phys. Rev. B **72**, 045136 (2005).
[20]G. van der Laan, Lect. Notes Phys. **697**, 143 (2006).
[21]B. T. Thole and G. van der Laan, Phys. Rev. B **44**, 12424 (1991).
[22]G. van der Laan and B. T. Thole, Phys. Rev. B **48**, 210 (1993).
[23]B. T. Thole and G. van der Laan, Phys. Rev. B **49**, 9613 (1994).
[24]G. van der Laan and B. T. Thole, Phys. Rev. B **43**, 13401 (1991).
[25]R. D. Cowan, *The Theory of Atomic Structure and Spectra* (University of California Press, Berkeley, CA, 1981).
[26]B. T. Thole, G. van der Laan, J. C. Fuggle, G. A. Sawatzky, R. C. Karnatak, and J. M. Esteva, Phys. Rev. B **32**, 5107 (1985).
[27]K. Starke, E. Navas, E. Arenholz, Z. Hu, L. Baumgarten, G. van der Laan, C. T. Chen, and G. Kaindl, Phys. Rev. B **55**, 2672 (1997).
[28]J. Terry, R. K. Schulze, J. D. Farr, T. Zocco, K. Heinzelman, E. Rotenberg, D. K. Shuh, G. van der Laan, D. A. Arena, and J. G. Tobin, Surf. Sci. **499**, L141 (2002).
[29]K. T. Moore, B. W. Chung, S. A. Morton, A. J. Schwartz, J. G. Tobin, S. Lazar, F. D. Tichelaar, H. W. Zandbergen, P. Soderlind, and G. van der Laan, Phys. Rev. B **69**, 193104 (2004).
[30]R. D. Cowan, *The Theory of Atomic Structure and Spectra* (University of California Press, Berkeley, CA, 1981), pp. 285 and 354.
[31]J. Sugar, Phys. Rev. B **5**, 1785 (1972).
[32]B. T. Thole, G. van der Laan, and M. Fabrizio, Phys. Rev. B **50**, 11466 (1994).
[33]B. T. Thole and G. van der Laan, Phys. Rev. B **38**, 3158 (1988).
[34]G. van der Laan and B. T. Thole, Phys. Rev. B **53**, 14458 (1996).
[35]J. L. Dehmer, A. F. Starace, U. Fano, J. Sugar, and J. W. Cooper, Phys. Rev. Lett. **26**, 1521 (1971).
[36]J. L. Dehmer and A. F. Starace, Phys. Rev. B **5**, 1792 (1972).
[37]H. Ogasawara, A. Kotani, and B. T. Thole, Phys. Rev. B **50**, 12332 (1994).
[38]G. van der Laan, E. Arenholz, E. Navas, A. Bauer, and G. Kaindl, Phys. Rev. B **53**, R5998 (1996).
[39]G. van der Laan and I. W. Kirkman, J. Phys.: Condens. Matter **4**, 4189 (1992).
[40]R. A. Gordon, G. T. Seidler, T. T. Fister, M. W. Haverkort, G. A. Sawatzky, A. Tanaka, and T. K. Sham, Europhys. Lett. **81**, 26004 (2008).
[41]G. van der Laan and M. Taguchi, Phys. Rev. B **82**, 045114 (2010).